

Chlorine activation and enhanced ozone depletion induced by wildfire aerosol

<https://doi.org/10.1038/s41586-022-05683-0>

Received: 9 August 2022

Accepted: 22 December 2022

Published online: 8 March 2023

 Check for updates

Susan Solomon^{1,7}✉, Kane Stone^{1,7}✉, Pengfei Yu², D. M. Murphy³, Doug Kinnison⁴, A. R. Ravishankara^{5,6} & Peidong Wang¹

Remarkable perturbations in the stratospheric abundances of chlorine species and ozone were observed over Southern Hemisphere mid-latitudes following the 2020 Australian wildfires^{1,2}. These changes in atmospheric chemical composition suggest that wildfire aerosols affect stratospheric chlorine and ozone depletion chemistry. Here we propose that wildfire aerosol containing a mixture of oxidized organics and sulfate^{3–7} increases hydrochloric acid solubility^{8–11} and associated heterogeneous reaction rates, activating reactive chlorine species and enhancing ozone loss rates at relatively warm stratospheric temperatures. We test our hypothesis by comparing atmospheric observations to model simulations that include the proposed mechanism. Modelled changes in 2020 hydrochloric acid, chlorine nitrate and hypochlorous acid abundances are in good agreement with observations^{1,2}. Our results indicate that wildfire aerosol chemistry, although not accounting for the record duration of the 2020 Antarctic ozone hole, does yield an increase in its area and a 3–5% depletion of southern mid-latitude total column ozone. These findings increase concern^{2,12,13} that more frequent and intense wildfires could delay ozone recovery in a warming world.

Massive wildfires in Australia during the austral summer of 2019–2020 (December–January) produced pyrocumulonimbus towers that released about 0.9 Tg of wildfire smoke into the stratosphere^{12,14}. Wildfires are also sometimes denoted as bushfires, wildland fires and forest fires; here we refer to them as wildfires. Wildfire smoke can be expected to be primarily composed of organic material, but its stratospheric chemistry is virtually unknown.

Wildfire aerosol composition and ageing

Airborne mass spectrometry data^{15–17} showed that carbonaceous compounds were frequently present in about 30–40% of individual particles in the background Northern Hemisphere tropopause and lowermost stratosphere region. The carbonaceous fraction was largely internally mixed with sulfate (that is, both sulfate and carbon were contained within single particles, although whether the latter took the form of a coating was not determined). Although the airborne instrument was not flown through the Australian event, wildfire smoke of the Pacific Northwest Event in 2017 showed about a doubling of the carbonaceous/sulfate aerosol population¹⁷.

Aged stratospheric smoke particles can be characterized by thick coatings¹⁸. Infrared satellite spectra of the stratospheric wildfire smoke particles after the 2020 event showed signatures of oxidized organic matter, in particular the OH and C=O stretch features^{2,19}. The smoke aerosols are referred to hereafter as organic.

Although the detailed composition of stratospheric smoke aerosols has not been determined, tropospheric studies provide insights at lower altitudes. Fresh tropospheric wildfire plumes contain a wide

variety of complex organic compounds, including, for example, furans and phenolic compounds, and large-molecular-weight species and humic-like substances can also be present²⁰. Levoglucosan is a marker for biomass-burning aerosols derived from the burning of cellulose and hemicellulose and is found in high concentrations in fresh tropospheric plumes²¹. But levoglucosan is oxidized in particles by, for example, reaction with OH, with a lifetime of about 1 day (ref. ²²), and secondary aerosol formation by other species is probably also important^{23,24}. Here fresh smoke need not be explicitly considered because we are interested in effects over timescales of weeks to months after the fires. The stratosphere is a highly oxidizing environment owing to high concentrations of ozone and free radicals.

There is strong observational evidence for oxidation of many of the complex organic species seen in fresh plumes in the troposphere. Tropospheric observations show a variety of alcohols and acids in aged smoke particles. A wide range of organic acids were identified in tropospheric smoke from Portuguese wildfires, including oleic acid (*cis*-9-octadecenoic acid), succinic acid, heptanedioic acid, malic acid and oxo-acids, as well as several methoxyphenols and alcohols; *n*-alkanols from C₁₀ to C₃₀ and *n*-alkanoic acids from C₆ to C₃₀ were also reported^{6,24}. Oxalic acid is frequently among the most abundant single species found in aged tropospheric wildfire smoke aerosols^{3–6,25,26}. It has been shown that organic acid content increased with smoke particle ageing and that carbohydrates such as levoglucosan are converted to organic acids during upward transport³. Aged aerosols from burning Australian vegetation have also been found to be hygroscopic and contain oxidized material⁷, although whether eucalyptus burning might produce different specific organics than other vegetation types merits further study.

¹Department of Earth, Atmospheric and Planetary Sciences, Massachusetts Institute of Technology, Cambridge, MA, USA. ²Institute for Environmental and Climate Research, Jinan University, Guangzhou, China. ³NOAA Chemical Sciences Laboratory, Boulder, CO, USA. ⁴Atmospheric Chemistry Observations and Modeling Laboratory, National Center for Atmospheric Research, Boulder, CO, USA. ⁵Department of Chemistry, Colorado State University, Fort Collins, CO, USA. ⁶Department of Atmospheric Science, Colorado State University, Fort Collins, CO, USA.

⁷These authors contributed equally: Susan Solomon, Kane Stone. ✉e-mail: solos@mit.edu; stonke@mit.edu

Whether stratospheric smoke is liquid, glassy or solid must also be considered. Although the Australian plume had a depolarized lidar signature in the stratosphere that generally indicates solid particles, it was partly owing to an unusual size distribution as well as soot in the plume, and can still be consistent with a population of liquid-like particles^{27–29}. Several recent papers suggest that organic aerosols may form glasses^{30–33}. However, complex mixtures of organics often take on liquid-like properties despite freezing or efflorescence behaviour in the individual components^{34,35}. Formation and maintenance of glasses can also be hindered by extra components (such as sulfate and nitrate) and for hygroscopic particles³⁶. Following the formalism discussed in Methods, we estimate a diffusive-reactive length scale in organic liquid surfaces on the order of 0.01 microns at mid-latitudes and in polar autumn, driven in large part by the high liquid solubility (hence high particulate concentration) of HCl discussed below. The high HCl abundance in the particle implies that reaction probably occurs very near the surface in particles on the order of a micron in size and reduces the influence of diffusion on the reaction rate. Note that, for stratospheric particles, continuing rapid fluxes of water from/to the surface and the atmosphere as well as the presence of HCl often lead to a quasi-liquid layer, even for solid ice particles (for example, ref. ³⁷). We suggest that the stratospheric smoke particles probably started out deliquesced as they ascended in the humid environment of dense pyrocumulonimbus clouds, then can be modelled as liquid-like at least for temperatures above about 195 K; we further assume that stratospheric wildfire particles contain large amounts of oxidized organics, particularly organic acids, along with sulfate.

Modelling and testing wildfire chemistry

A sectional aerosol microphysics model (Community Aerosol and Radiation Model for Atmospheres (CARMA)) coupled with the Community Earth System Model (CESM) has been shown to simulate both the observed sulfate and organic/sulfate populations of background lower stratospheric particles^{38,39}. The application of this model to the 2020 wildfires reproduced both the observed heating of the stratosphere¹² and effects on NO_x chemistry by means of the N₂O₅ + H₂O heterogeneous reaction¹³. Extended Data Fig. 1 shows that the calculated and observed latitudinal and temporal spread of aerosol extinction during and after the 2020 wildfires are in good general agreement at, for example, 18.5 km; see also ref. ¹². Here we use a specified dynamics version of this state-of-the-art microphysics/atmospheric chemistry model (see Methods). The use of specified dynamics based on observations precludes study of dynamical or radiative feedbacks but allows clear identification of the chemical effects of different chemical processes.

Most of the chlorine released from chlorofluorocarbons resides in HCl and ClONO₂ in the lower stratosphere. The influence of organic/sulfate particles on stratospheric chlorine chemistry (such as that of background and volcanic aerosol composed of sulfate/water particles, as well as polar stratospheric clouds (PSCs)) can be expected to be linked to the dissolution and heterogeneous reactions of these species⁴⁰. The most important chlorine processing reactions in/on stratospheric sulfate are



The rates of these reactions in/on liquid sulfate particles are heavily dependent on temperature and water vapour partial pressure, which

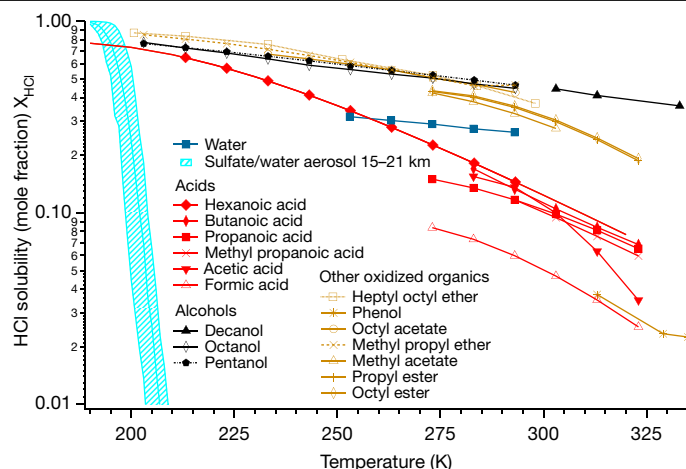


Fig. 1 | HCl solubility in different liquids. Solubility (in mole fraction) of HCl in various organics, pure water and sulfate/water mixtures is shown as a function of temperature based on available laboratory data. The values shown for sulfate/water mixtures are for typical stratospheric conditions over the height range from about 15 to 21 km and are taken from the model used here.

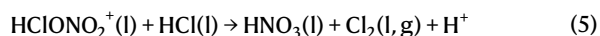
control the acidity and hence the solubility of the reactants, particularly HCl (ref. ⁴¹). They are most effective on PSCs in the cold polar region at temperatures below about 195 K (see Fig. 1), at which they take on water and HCl solubility increases. The above heterogeneous reactions can rapidly deplete HCl (and ClONO₂), generating ClO and Cl₂O₂ and leading to the Antarctic ozone hole. The observed large 2020 mid-latitude decrease in HCl at much warmer mid-latitude temperatures suggests that HCl dissolution in mixed organic/sulfate smoke should be considered.

There is an extensive literature on HCl solubility in non-aqueous solvents dating to at least the 1930s⁴², owing to interest in basic physical chemistry questions such as the role of the dipole moment in the solubility process. Many more studies were published after the 1940s, in part linked to growth in industrial uses of HCl, for example, in syntheses of various plastics and synthetic rubber. Illustrative examples of measured HCl solubility (mole fraction units)^{8–11} versus temperature are presented in Fig. 1 for various types of oxidized organic species that may be present in wildfire smoke; pure liquid water and liquid sulfate/water solutions are also shown for reference. The figure demonstrates that HCl is as (or more) soluble in many types of oxidized organic (ranging across alcohols, ethers, esters and acids) than in water at temperatures below about 260 K; it is far more soluble in oxidized organics than in the background pure sulfate/water or PSC particles of the stratosphere unless temperatures fall below about 200 K (for example, in the Antarctic in winter and spring).

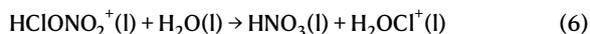
The reported solubility of HCl in formic acid (HCOOH) is lower than in the larger organic acids, but the higher-molecular-weight acids (C₃ and greater) show very similar values to one another, with increases at colder temperatures that approach those in the alcohols. The only organic acid for which solubility data below 220 K are available in the published literature is hexanoic acid. Because C₃ and larger oxidized organic acids are probably the main components of aged stratospheric wildfire particles (as they are in the troposphere), here we adopt the solubility of HCl and its temperature dependence in hexanoic acid to approximately represent particulate oxidized organic matter in our numerical model calculations (see Methods). If, for example, more oxidized alcohols or ethers were present in the particles than acids, this would probably increase the HCl solubility slightly.

Because HCl is substantially more soluble in a wide variety of organics at temperatures above about 200 K than it is in background sulfate/water particles based on available laboratory studies (Fig. 1), these data

point towards a transformative role in mid-latitude stratospheric chemistry when oxidized organic aerosols are present. Although alternative elementary reactions are possible, an acid-catalysed mechanism has been proposed^{41,43} for reactions (1) and (2):



The high solubility of HCl in oxidized organics (Fig. 1) indicates that reaction (5) should occur readily at stratospheric temperatures. This process competes with the first step of reaction (2):



The high solubility of HCl in organic acids suggests that the available $\text{HCIONO}_2^+(\text{l})$ should be more likely to react with $\text{HCl}(\text{l})$ than with $\text{H}_2\text{O}(\text{l})$ in mixed organic/sulfate particles following this mechanism. This is consistent with the known reactivities of reactions (1) and (2) in liquid sulfate aerosols as HCl solubility and hence HCl(l) concentrations increase at cold temperatures below about 195 K, enhancing reaction (1) while suppressing reaction (2); by contrast, reaction (2) is faster than reaction (1) in sulfate particles at warmer temperatures⁴¹. Reactions (3) and (4) would also be enhanced by high concentrations of HCl(l) and are included here.

To explore the influence of HCl solubility in wildfire particles, we carried out several tests. In one test, we use the HCl solubility in hexanoic acid data (hereafter referred to as solubility case) of Fig. 1 as approximately representative for the oxidized organic/sulfate particles (see Methods), which greatly increases the rates of reactions (1), (3) and (4) at warmer temperatures >200 K. In a second test, we treat the liquid organic portion of the particles like water at all temperatures, that is, we simply impose a dilution factor (dilution case) proportional to the organic content of the organic/sulfate/water particles. This alters the computed H_2SO_4 mole fraction and affects not only reactions (1), (3) and (4) but also reaction (2). This could occur, for example, if the mechanism delineated in reactions (5) and (6) is not valid, enhancing the potential rate of the $\text{ClONO}_2 + \text{H}_2\text{O}$ reaction. In all wildfire model tests, smoke input changes the amount of total aerosol and its associated surface area, enhancing the $\text{N}_2\text{O}_5 + \text{H}_2\text{O}$ reaction rate; in a third test, only that process is considered on the wildfire aerosols¹³ to compare ozone depletion contributions from different processes (N_2O_5 only case). We compare these three tests to a control run that includes no organic particle chemistry (no organics case).

We find that the model-calculated anomalies in chlorine species for the oxidized organics solubility case are in remarkable agreement overall with the unprecedented extreme changes seen in the 2020 southern mid-latitude observations (Fig. 2). Observed 2020 changes in ozone, HCl, ClONO_2 and ClO at 68 hectopascals (hPa) relative to the climatological averages and ranges of available observations for previous years from the Microwave Limb Sounder (MLS) and the Atmospheric Chemistry Experiment (ACE) satellite instruments are presented. Model results are 24-h daily averages, whereas observations shown are averages of available data (sunrise and sunset monthly averages for ACE; averages of daily day and nighttime orbits for MLS). Corresponding absolute values for 2020 and the pre-2020 climatologies are shown in Extended Data Fig. 2. HOCl is also reported by ACE but is subject to greater uncertainty, and its anomalies and absolute concentrations are shown in Extended Data Fig. 3. The consistency between the model and measurements obtained across the various species, and over time during the year, strongly supports the proposed mechanism. Differences in absolute abundances probably largely reflect shortcomings in the transport processes of the model.

By contrast, the dilution case greatly overestimates the initial ClO (and HOCl) increases and, accordingly, results in too much ozone loss (Fig. 2). In this case, reaction (2) is enhanced and then declines following

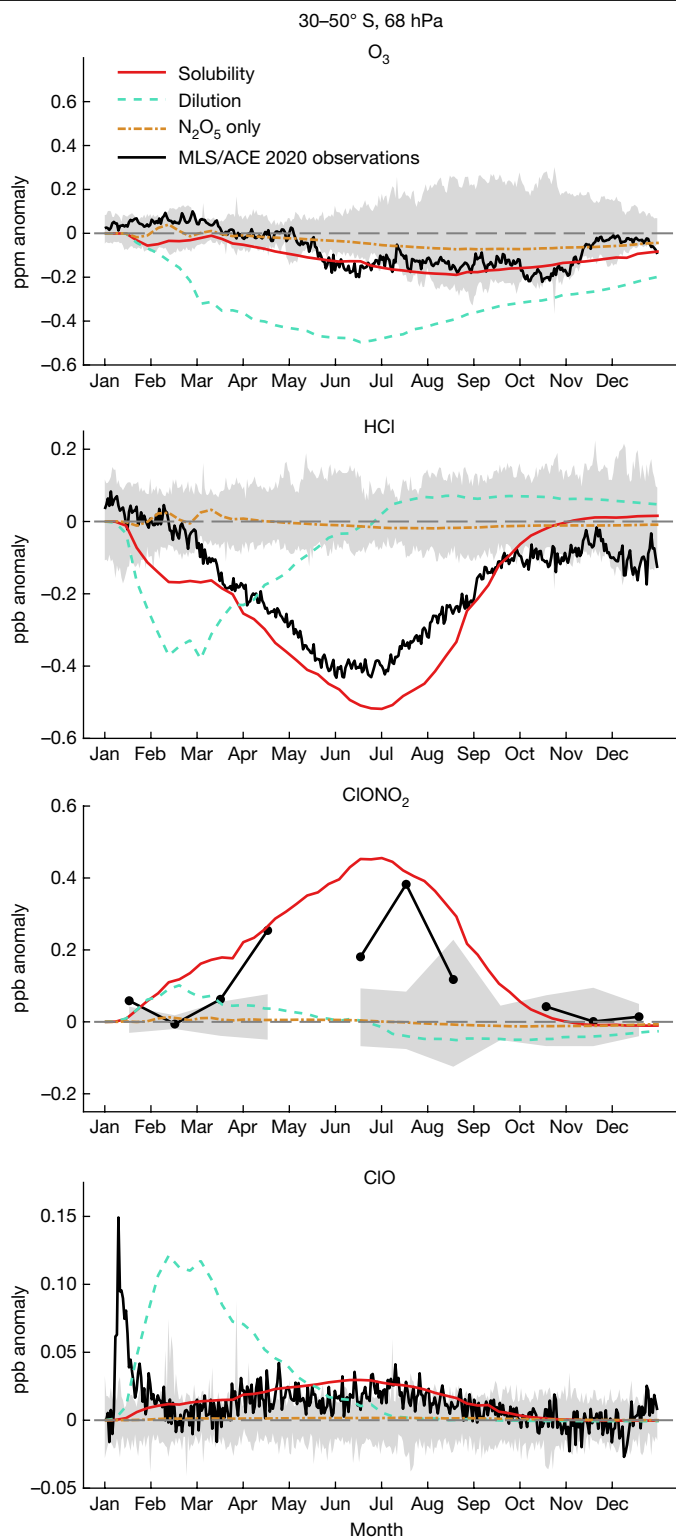


Fig. 2 | Observed and modelled 2020 anomalies in chemical species from 30–50° S at 68 hPa. Grey shaded regions show the ranges of 24-h averaged satellite data anomalies relative to the climatologies of satellite observations before 2020 (daily O_3 , HCl and ClO from MLS and monthly ClONO_2 from ACE), whereas black lines show the observed anomalies for 2020. Other coloured lines denote calculated anomalies relative to the modelled no organics control for three model test cases: including only N_2O_5 hydrolysis on the aerosols (dashed brown line), considering the added organic material as a dilution factor (dashed green line) and considering the adopted solubility of HCl in organic particles (red line). ppb, parts per billion (by volume throughout this paper); ppm, parts per million (by volume throughout this paper).

the wildfire particle abundances. The fast rate of reaction (2) leads to reduced rather than enhanced autumn ClONO₂, as observed.

Taken together, these results indicate that atmospheric HCl indeed dissolves readily in smoke particles under stratospheric conditions, in a manner that is well captured by available solubility data in oxidized organics. This yields subsequent rapid reactions of HCl with ClONO₂, HOCl, and HOBr in the particles at relatively warm mid-latitude temperatures, with reaction (1) being the dominant process in the present model. On the basis of the dilution case, it seems that the ClONO₂ + H₂O reaction is suppressed relative to the ClONO₂ + HCl reaction in these particles.

In contrast to HCl, satellite measurements indicate that stratospheric nitric acid was not markedly perturbed by the Australian smoke⁴⁴ and the model is consistent with those data (Extended Data Fig. 4). High values of ClONO₂ are maintained in the sunlit atmosphere in the solubility case, limiting the potential for ozone loss despite a rapid heterogeneous rate for reaction (1). This is owing to continuing HNO₃ photolysis and reaction with OH, leading to reduced but non-zero values of observed NO₂ (ref. 40) and hence reformation of ClONO₂. Thus, a different balance is obtained in mid-latitudes compared with the cold and dark polar regions, in which essentially no NO₂ is available to reform ClONO₂ after heterogeneous loss, allowing far greater ClO anomalies to build up and form the ozone hole⁴⁰. Nonetheless, ClONO₂ itself photolyses rapidly and is approximately in photochemical steady state with ClO under sunlit mid-latitude conditions, so increased ClONO₂ as seen in Fig. 2 implies that some increases in ClO and ozone loss must occur. The shifts in chlorine chemistry result in a threefold calculated increase in ClO, consistent with observations, and this leads to most of the peak local ozone depletion of 10–20% during May to December as shown, which is in accord with the record-low local ozone in this region in June according to the data (Fig. 2). Extended Data Fig. 5 shows that the observed ozone loss profiles on coincident days of observation are similar between ACE and MLS for June–July as an example comparison.

Vertical anomaly profiles of HCl, ClO and ClONO₂ averaged over all available data and all model days for June–July 2020 at southern mid-latitudes are also fairly well captured by the solubility case, albeit with some overestimates at higher pressures (lower altitudes), further supporting the proposed mechanism through its links to the profile of wildfire aerosols (Fig. 3). As in Fig. 2, the data do not agree with the model dilution case. Corresponding absolute values are shown in Extended Data Fig. 6.

The model suggests that the wildfire aerosols chemically deplete the mid-latitude total ozone column from 30–50° S by up to 18 Dobson units (DU), roughly triple the amount obtained from N₂O₅ hydrolysis alone, yielding about 3–5% total chemical column loss depending on the month of 2020. Such changes are relatively small compared with the effects of interannual dynamical variability at mid-latitudes and there is evidence for some dynamically driven decreases in ozone in 2020 (refs. 1,45). Recent studies suggest that the radiative perturbations linked to wildfire smoke affected 2020 Southern Hemisphere dynamical conditions and possibly ozone, which could represent feedbacks in addition to the direct chemical effects evaluated here^{46,47}. Nevertheless, the chemical changes are substantial in comparison with the 1% per decade increase expected owing to long-term decreases in halocarbons that have occurred under the international Montreal Protocol and indicate that delays in ozone recovery could occur if wildfires become more frequent or intense in the future.

Some studies have speculated that wildfires may deplete polar ozone⁴⁸. The Antarctic ozone hole of 2020 was both large in area and of record duration (lasting through late December)⁴⁹. In sharp contrast with mid-latitudes, we find that the observed polar 2020 abundances of ozone, HCl, ClONO₂ and ClO for 68 hPa from 70–80° S show few marked departures from the ranges of previous years (Fig. 4). The small influence of our wildfire chemistry mechanism on ozone losses in Antarctic spring can be expected because the adopted solubility of HCl in organics becomes smaller than that of typical liquid PSCs

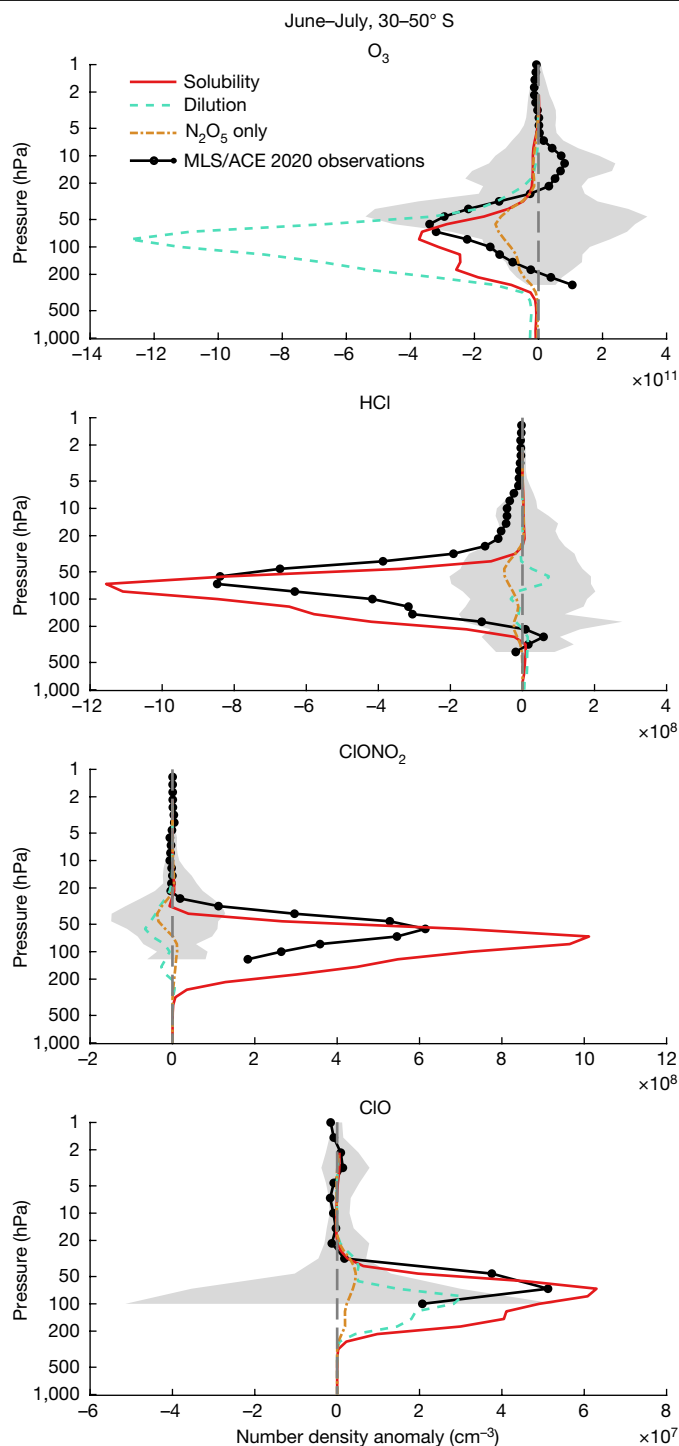


Fig. 3 | Observed and modelled vertical profile anomalies in chemical species from 30–50° S in June–July 2020. Grey shaded regions show the ranges of 24-h averaged satellite data anomalies relative to the climatologies of satellite observations before 2020 (daily O₃ and ClO from MLS and HCl and ClONO₂ from ACE, with coverage to low altitudes), whereas black lines show observed anomalies for 2020. Other coloured lines denote calculated anomalies relative to the modelled no organics control for three model test cases: including only N₂O₅ hydrolysis on the aerosols (dashed brown line), considering the added organic material as a dilution factor (dashed green line) and considering the adopted solubility of HCl in organic particles (red line).

below about 200 K (Fig. 1), that is, in polar winter and spring when the ozone hole forms. Larger local ozone changes are obtained close to the tropopause (that is, 100–200 hPa; see Extended Data Fig. 7), at which

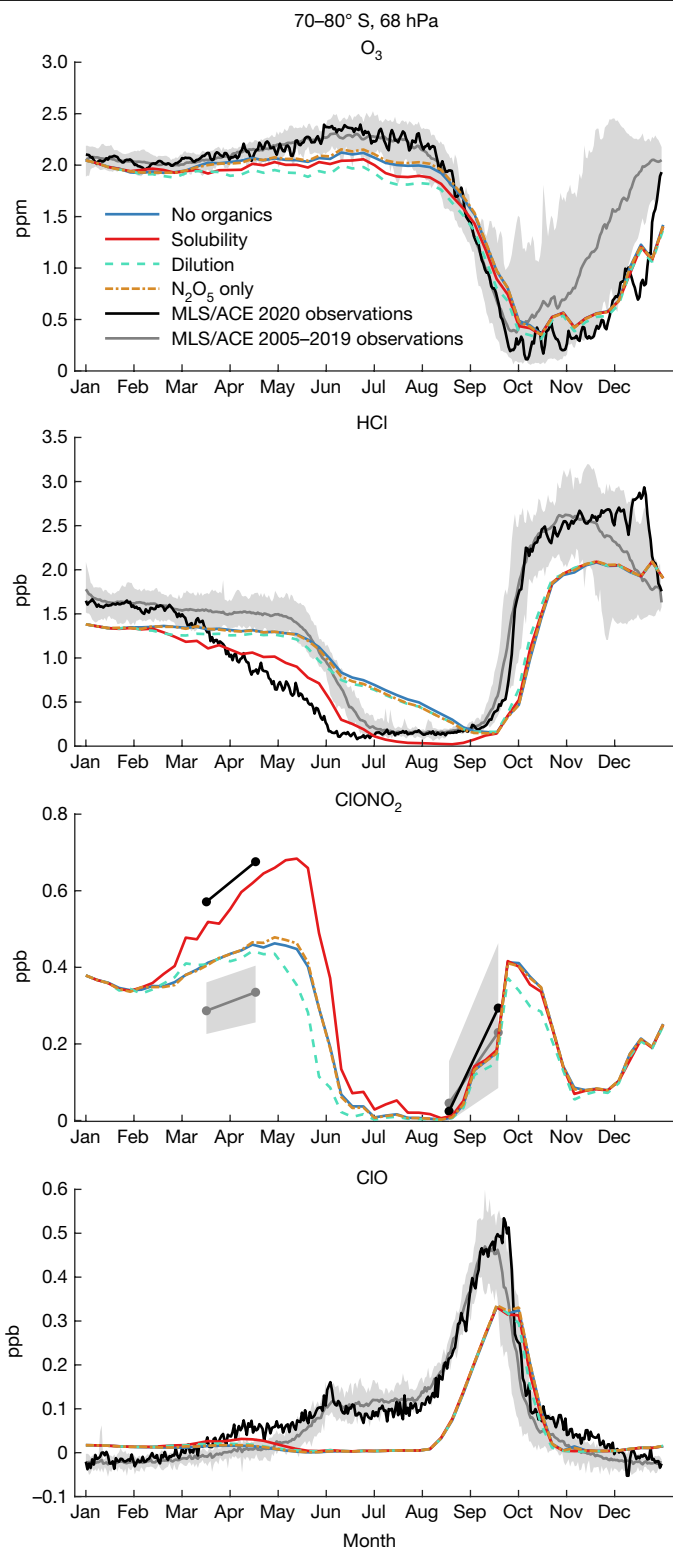


Fig. 4 | Observed and modelled mixing ratios of chemical species at 70–80° S, 68 hPa. Grey shaded regions show the ranges of 24-h averaged satellite data (daily O₃, HCl and ClO from MLS and monthly ClONO₂ from ACE) for previous years and the grey line shows their averages, whereas black lines show observations for 2020. Other coloured lines show model-calculated abundances for the no organics control run and for three model test cases: including only N₂O₃ hydrolysis on the aerosols (dashed brown line), considering the added organic material as a dilution factor (dashed green line) and considering the adopted solubility of HCl in organic acid particles (red line).

temperatures are too warm for PSCs. However, the concentration of ozone is relatively small at these altitudes, so the effect on the polar total column depletion is modest (about 5% of the integrated column), much less than that driven by PSCs at higher altitudes.

Notably, observed 2020 polar HCl abundances in the austral autumn season (April–May) decline far earlier (Fig. 4) than in any other year and the oxidized organics solubility case of the model broadly reproduces this unusual behaviour. Temperatures at these latitudes and times are comparable with those in mid-latitudes, so this is to be expected through the added chemistry. The observed HCl inside the polar vortex is also effectively entirely removed by June–July in 2020, considerably lower than the no organics control case or data in other years (Fig. 4 and maps in Extended Data Fig. 8).

A long-standing puzzle in stratospheric chemistry is that the observed timing of early winter HCl decline in the Antarctic and occasionally in the Arctic typically occurs earlier than models predict (see the comprehensive review in ref.⁵⁰), as illustrated in Fig. 4 and Extended Data Fig. 8 for the no organics control case of this model (similar to other models)⁵⁰. Our simulations raise the question of whether early polar winter HCl declines could be linked to background levels of organic particles^{15–17} in non-wildfire years.

Although the early winter HCl discrepancy phenomenon is of long-standing chemical interest, our results provide further evidence that it causes limited changes in calculated Antarctic total column ozone depletion in this region³⁹. Indeed, the control no organics and organics runs both simulate the 70–80° S 2020 ozone losses and their record long duration well (Fig. 4), implying a dominant role for the observed unusually cold conditions in that year (as imposed on the basis of a reanalysis in these simulations). Inclusion of the wildfire organics HCl solubility does, however, expand the calculated area of the ozone hole (defined as the region in which total column ozone is less than 220 DU) compared with the no organics control by about 2.5 million km² in September–October of 2020, contributing to the unusually large ozone hole in that year.

Wildfire aerosol in a warming world

Here we have shown that the effect of wildfire smoke on stratospheric chemistry consists not only of increases in particle surface area (as has been assumed in the published literature)^{12,13,45} but, more importantly, in profound impacts on HCl solubility and reactivity. In particular, the 2020 Southern Hemisphere mid-latitude lower stratospheric composition extremes in HCl, ClONO₂, ClO and HOCl are remarkably well reproduced by a model that considers the extremely high solubility of HCl in oxidized wildfire smoke organics at warm stratospheric temperatures (as indicated by historical laboratory solubility data) and subsequent reactions. These in turn deplete mid-latitude ozone.

A record-early observed 2020 southern autumn (April–May) disappearance of HCl at 70–80° S is another finding of this paper and is well simulated by this model. Whether the smaller amounts of organic particles present in other years may be responsible for discrepancies between calculated and observed HCl declines⁵⁰ in high-latitude autumn and winter documented in the published literature merits future study.

Although the model indicates that the organic particles expanded the size of the September–October 2020 ozone hole by about 2.5 million km², it does not explain its record longevity⁴⁹, raising the question of the roles of natural variability and possible forcings (for example, relation to the unusual mid-latitude ozone losses as well as the radiative effects of the particles themselves and resulting impacts on temperatures, winds and stratosphere–troposphere coupling^{46,47,49}). Further work is needed to examine potential radiative and dynamical feedbacks of the aerosol and ozone changes.

The same chemistry discussed here for the southern mid-latitudes and polar regions can also be expected in Northern Hemisphere wildfire smoke. Further, similar reactions should occur wherever aged organic

aerosols and HCl are found, that is, not only in wildfire smoke but also in biomass burning, pollution and, potentially, aircraft-generated aerosols, both in the lower stratosphere and in the troposphere. Consequences of HCl solubility in oxidized organics for long-term lower stratospheric ozone trends also merit further study, along with potentially altered solubilities of other compounds besides HCl in such particles in tropospheric and stratospheric chemistry.

In closing, limitations of our chemical assumptions should be noted. For example, it is possible that the organic material could freeze, even doing so at warmer temperatures than normal, and thereby prolonging heterogeneous chemistry in polar spring (and possibly autumn). Other reactions beyond those considered may also be important, and new laboratory studies of solubility and reactions of stratospheric species in oxidized organic aerosols and especially wildfire aerosols are desperately needed if, as expected, wildfire frequency and intensity increase in a warming world.

Online content

Any methods, additional references, Nature Portfolio reporting summaries, source data, extended data, supplementary information, acknowledgements, peer review information; details of author contributions and competing interests; and statements of data and code availability are available at <https://doi.org/10.1038/s41586-022-05683-0>.

- Santee, M. L. et al. Prolonged and pervasive perturbations in the composition of the Southern Hemisphere midlatitude lower stratosphere from the Australian New Year's fires. *Geophys. Res. Lett.* **49**, e2021GL096270 (2022).
- Bernath, P., Boone, C. & Crouse, J. Wildfire smoke destroys stratospheric ozone. *Science* **375**, 1292–1295 (2022).
- Gao, S. et al. Water-soluble organic components in aerosols associated with savanna fires in Southern Africa: identification, evolution, and distribution. *J. Geophys. Res.* **108**, 8491 (2003).
- Kundu, S., Kawamura, K., Andreae, T. W., Hoffer, A. & Andreae, M. O. Molecular distributions of dicarboxylic acids, ketocarboxylic acids and α -dicarbonyls in biomass burning aerosols: implications for photochemical production and degradation in smoke layer. *Atmos. Chem. Phys.* **10**, 2209–2225 (2010).
- Trebs, I. et al. Real-time measurements of ammonia, acidic trace gases and water-soluble inorganic aerosol species at a rural site in the Amazon Basin. *Atmos. Chem. Phys.* **4**, 967–987 (2004).
- Vicente, A. et al. Organic speciation of aerosols from wildfires in central Portugal during summer 2009. *Atmos. Environ.* **57**, 186–196 (2012).
- Mallet, M. D. et al. Composition, size and cloud condensation nuclei activity of biomass burning aerosol from northern Australian savannah fires. *Atmos. Chem. Phys.* **17**, 3605–3617 (2017).
- Ahmed, W., Gerrard, W. & Malukdar, V. K. Significance of the solubility of hydrogen halides in liquid compounds. *J. Appl. Chem.* **20**, 109–116 (1970).
- Gerrard, W. & Macklen, E. Solubility of hydrogen halides in organic compounds containing oxygen. I. Solubility of hydrogen chloride in alcohols, carboxylic acids and esters. *J. Appl. Chem.* **6**, 241–244 (1956).
- Gerrard, W., Mincer, A. M. A. & Wyvill, P. L. Solubility of hydrogen halides in organic compounds containing oxygen. III. Solubility of hydrogen chloride in alcohols and certain esters at low temperatures. *J. Appl. Chem.* **9**, 89–93 (1959).
- International Union of Pure and Applied Chemistry (IUPAC), Fogg, P. G. T., Gerrard, W. & Clever, H. L. (eds) *Hydrogen Halides in Non-aqueous Solvents (Solubility Data Series)* Vol. 42 (Pergamon, 1990).
- Yu, P. et al. Persistent stratospheric warming due to 2019–2020 Australian wildfire smoke. *Geophys. Res. Lett.* **48**, e2021GL092609 (2021).
- Solomon, S. et al. On the stratospheric chemistry of midlatitude wildfire smoke. *Proc. Natl Acad. Sci. USA* **119**, e2117325119 (2022).
- Peterson, D. A. et al. Australia's Black Summer pyrocumulonimbus super outbreak reveals potential for increasingly extreme stratospheric smoke events. *NPJ Clim. Atmos. Sci.* **4**, 38 (2021).
- Murphy, D. M., Thomson, D. S. & Mahoney, M. J. In situ measurements of organics, meteoritic material, mercury, and other elements in aerosols at 5 to 19 kilometers. *Science* **282**, 1664–1669 (1998).
- Murphy, D. M., Cziczo, D. J., Hudson, P. K. & Thomson, D. S. Carbonaceous material in aerosol particles in the lower stratosphere and tropopause region. *J. Geophys. Res.* **112**, D04203 (2007).
- Murphy, D. M. et al. Radiative and chemical implications of the size and composition of aerosol particles in the existing or modified global stratosphere. *Atmos. Chem. Phys.* **21**, 8915–8932 (2021).
- Ditas, J., Ma, N., Zhang, Y. & Cheng, Y. Strong impact of wildfires on the abundance and aging of black carbon in the lowermost stratosphere. *Proc. Natl Acad. Sci. USA* **115**, E11595–E11603 (2018).
- Boone, C. D., Bernath, P. F. & Fromm, M. D. Pyrocumulonimbus stratospheric plume injections measured by the ACE-FTS. *Geophys. Res. Lett.* **47**, e2020GL088442 (2020).
- Palm, B. B., Peng, Q., Fredrickson, C. D. & Thornton, J. A. Quantification of organic aerosol and brown carbon evolution in fresh wildfire plumes. *Proc. Natl Acad. Sci. USA* **117**, 29469–29477 (2020).
- Sannigrahi, P., Sullivan, A. P., Weber, R. J. & Ingall, E. D. Characterization of water-soluble organic carbon in urban atmospheric aerosols using solid-state ^{13}C NMR spectroscopy. *Environ. Sci. Technol.* **40**, 666–672 (2006).
- Garofalo, L. A. et al. Emission and evolution of submicron organic aerosol in smoke from wildfires in the western United States. *ACS Earth Space Chem.* **3**, 1237–1247 (2019).
- Cappa, C. D. et al. Biomass-burning-derived particles from a wide variety of fuels – part 2: effects of photochemical aging on particle optical and chemical properties. *Atmos. Chem. Phys.* **20**, 8511–8532 (2020).
- Vicente, A. et al. Emission factors and detailed chemical composition of smoke particles from the 2010 wildfire season. *Atmos. Environ.* **71**, 295–303 (2013).
- Mochida, M. et al. Spatial distributions of oxygenated organic compounds (dicarboxylic acids, fatty acids, and levoglucosan) in marine aerosols over the western Pacific and off the coast of East Asia: continental outflow of organic aerosols during the ACE-Asia campaign. *J. Geophys. Res. Atmos.* **108**, 8638 (2003).
- Deshmukh, D. K. et al. High loadings of water-soluble oxalic acid and related compounds in PM_{2.5} aerosols in eastern central India: influence of biomass burning and photochemical processing. *Aerosol Air Qual. Res.* **19**, 2625–2644 (2019).
- Haarig, M. et al. Depolarization and lidar ratios at 355, 532, and 1064 nm and microphysical properties of aged tropospheric and stratospheric Canadian wildfire smoke. *Atmos. Chem. Phys.* **18**, 11847–11861 (2018).
- Ohneiser, K. et al. Smoke of extreme Australian bushfires observed in the stratosphere over Punta Arenas, Chile, in January 2020: optical thickness, lidar ratios, and depolarization ratios at 355 and 532 nm. *Atmos. Chem. Phys.* **20**, 8003–8015 (2020).
- Ansmann, A. et al. Tropospheric and stratospheric wildfire smoke profiling with lidar: mass, surface area, CCN, and INP retrieval. *Atmos. Chem. Phys.* **21**, 9779–9807 (2021).
- Zobrist, B., Marcolli, C., Pedenera, D. A. & Koop, T. Do atmospheric aerosols form glasses? *Atmos. Chem. Phys.* **8**, 5221–5244 (2008).
- Virtanen, A. et al. An amorphous solid state of biogenic secondary organic aerosol particles. *Nature* **467**, 824–827 (2010).
- Reid, J. P. et al. The viscosity of atmospherically relevant organic particles. *Nat. Commun.* **9**, 956 (2018).
- Boomer, V. et al. Sunlight can convert atmospheric aerosols into a glassy solid state and modify their environmental impacts. *Proc. Natl Acad. Sci. USA* **119**, e2208121119 (2022).
- Cappa, C. D., Lovejoy, E. R. & Ravishankara, A. R. Evidence for liquid-like and nonideal behavior of a mixture of organic aerosol components. *Proc. Natl Acad. Sci. USA* **105**, 18687–18691 (2008).
- Marcolli, C., Luo, B. P. & Peter, T. Mixing of the organic aerosol fractions: liquids as the thermodynamically stable phases. *J. Phys. Chem. A* **108**, 2216–2224 (2004).
- Koop, T., Bookhold, J., Shirawa, M. & Poeschl, U. Glass transition and phase state of organic compounds: dependency on molecular properties and implications for secondary organic aerosols in the atmosphere. *Phys. Chem. Chem. Phys.* **13**, 19238–19255 (2011).
- McNeill, V. F., Loerting, T., Geiger, F. M., Trout, B. L. & Molina, M. J. Hydrogen chloride-induced surface disordering on ice. *Proc. Natl Acad. Sci. USA* **103**, 9422–9427 (2006).
- Yu, P. et al. Evaluations of tropospheric aerosol properties simulated by the community earth system model with a sectional aerosol microphysics scheme. *J. Adv. Model. Earth Syst.* **7**, 865–914 (2015).
- Yu, P. et al. Radiative forcing from anthropogenic sulfur and organic emissions reaching the stratosphere. *Geophys. Res. Lett.* **43**, 9361–9367 (2016).
- Solomon, S. Stratospheric ozone depletion: a review of concepts and history. *Rev. Geophys.* **37**, 275–316 (1999).
- Shi, Q., Jayne, J. T., Kolb, C. E., Worsnop, D. R. & Davidovits, P. Kinetic model for reaction of ClONO₂ with H₂O and HCl and HOCl with HCl in sulfuric acid solutions. *J. Geophys. Res.* **106**, 24259–24274 (2001).
- Bell, R. P., The electrical energy of dipole molecules in solution, and the solubilities of ammonia, hydrogen chloride, and hydrogen sulphide, in various solvents. *J. Chem. Soc. https://doi.org/10.1039/JR9310001371* (1931).
- Robinson, G. N., Worsnop, D. R., Jayne, J. T., Kolb, C. E. & Davidovits, P. Heterogeneous uptake of ClONO₂ and N₂O₅ by sulfuric acid solutions. *J. Geophys. Res.* **102**, 3583–3601 (1997).
- Schwartz, M. J. et al. Australian New Year's pyroCb Impact on stratospheric composition. *Geophys. Res. Lett.* **47**, e2020GL090831 (2020).
- Strahan, S. E. et al. Unexpected repartitioning of stratospheric inorganic chlorine after the 2020 Australian wildfires. *Geophys. Res. Lett.* **49**, e2022GL098290 (2022).
- Yook, S., Thompson, D. W. J. & Solomon, S. Climate impacts and potential drivers of the unprecedented Antarctic ozone holes of 2020 and 2021. *Geophys. Res. Lett.* **49**, e2022GL098064 (2022).
- Damany-Pearce, L. et al. Australian wildfires cause the largest stratospheric warming since Pinatubo and extends the lifetime of the Antarctic ozone hole. *Sci. Rep.* **12**, 12665 (2022).
- Ohneiser, K. et al. The unexpected smoke layer in the High Arctic winter stratosphere during MOSAIC 2019–2020. *Atmos. Chem. Phys.* **21**, 15783–157808 (2021).
- Klekociuk, A. R. et al. The Antarctic ozone hole during 2020. *J. South. Hemisph. Earth Syst. Sci.* **72**, 19–37 (2022).
- Grooß, J.-U. et al. On the discrepancy of HCl processing in the core of the wintertime polar vortices. *Atmos. Chem. Phys.* **18**, 8647–8666 (2018).

Publisher's note Springer Nature remains neutral with regard to jurisdictional claims in published maps and institutional affiliations.

Springer Nature or its licensor (e.g. a society or other partner) holds exclusive rights to this article under a publishing agreement with the author(s) or other rightsholder(s); author self-archiving of the accepted manuscript version of this article is solely governed by the terms of such publishing agreement and applicable law.

© The Author(s), under exclusive licence to Springer Nature Limited 2023

Methods

Model simulations

We use the sectional aerosol model CARMA coupled with the National Science Foundation/Department of Energy CESM (CESM-CARMA)^{38,39,51,52}. We spin-up by running the model from a multiyear free-running simulation and continue in free-running mode from 29 December 2019 to 1 March 2020, which allows the initial injection to be self-lofted into the stratosphere, as shown in ref.¹². We inject 0.9 Tg of smoke (three times that of the Pacific Northwest fires in 2017) during the fire days of 29–31 December 2019 and 4 January 2020 over southeastern Australia (39° S, 150° E) at an altitude of 12 km (ref.¹²). The smoke is made up of 2.5% black carbon, which is a factor in the lofting of the injected smoke; sensitivity simulations with other values in this model¹² show that this percentage gave the best match to satellite observations in this model. After 1 March, simulated winds and temperatures are nudged to the Goddard Earth Observing System version 5 analysis (GEOS-5)⁵³ to ensure accurate meteorological conditions for 2020 that are insensitive to the upper boundary and optimize comparisons with observations.

The model includes 56 layers from the surface up to 1.8 hPa (about 45 km), with a vertical resolution of about 1 km in the upper troposphere and lower stratosphere. The horizontal resolution of the model is 1.9° latitude × 2.5° longitude.

The model calculates two kinds of organic aerosols: (1) organic material mixed with sulfate, black carbon, sea salt and dust and (2) purely organic smoke particles emitted from the fires. Both sets of particles are computed in 20 size bins whose radii range from 0.05 to 8.7 μm. The model includes both the oxidation of the organic component of the smoke by ozone and condensation of sulfuric acid on the smoke particles¹².

Stratospheric heterogeneous chemistry rates in and on aerosols are calculated using the kinetics parameterization approach generally used in atmospheric chemistry models⁴¹ for the heterogeneous reactions of ClONO₂ + HCl, ClONO₂ + H₂O and HOCl + HCl. The kinetics approach uses experimental data for HCl, HOCl and ClONO₂ liquid diffusion, solubility and reactivity to obtain the heterogeneous reactions for H₂SO₄/H₂O stratospheric aerosol heterogeneous kinetics.

To investigate the effect of smoke on stratospheric chemistry, four model setups are used that adopt different heterogeneous chemistry on stratospheric aerosols. Further detail on the oxidized organic HCl solubility and dilution cases (see main text) is given in the following.

Dilution. This simulation assumes that the organic carbon behaves as an aerosol diluent and combines with the H₂SO₄/H₂O aerosols, which effectively lowers the H₂SO₄ weight percent that is a key parameter in the kinetics parameterization⁴¹. This is achieved by

$$\text{wt}_d = \frac{1}{\frac{1}{\text{wt}} + \frac{\text{OC}}{\text{SO}_4}}$$

in which wt is the weight percent of H₂SO₄ in the H₂SO₄/H₂O solution, wt_d is the diluted H₂SO₄ weight percent, OC is the organic carbon mass concentration and SO₄ is the sulfur mass concentration. An estimate of the organic molar mass of 116 (hexanoic acid) is used to obtain the organic-weight-corrected H₂SO₄ mole fraction as follows

$$x_{\text{H}_2\text{SO}_4} = \frac{\text{wt}_d}{\text{wt}_d + \frac{\text{wt}_{\text{H}_2\text{O}} \times 98}{18} + \frac{\text{wt}_{\text{OC}} \times 98}{116}}$$

which is then used in the calculation of HCl solubility. Here wt_{H₂O} and wt_{OC} are the weight percent of water and organic carbon, respectively, 98 is the molar mass of H₂SO₄, 18 is the molar mass of H₂O and 116 is the molar mass of hexanoic acid.

Solubility. This simulation alters the HCl solubility to account for the effects of smoke organics using laboratory measurements^{8–11} (instead

of changing the H₂SO₄ weight percent). This is done for all locations and times when the ratio of mass concentration of organic carbon to sulfur is >1; otherwise, the original parameterization⁴¹ is used. Following ref.¹¹, the HCl mole fraction in hexanoic acid is calculated using the following fit function to the laboratory data points (see red diamonds in Fig. 1, in which the red line through them indicates this fit):

$$x_{\text{HCl}} = \exp\left(28.99 - \frac{3,300.46}{T} - 18.14 \times \log\left(\frac{T}{100}\right)\right)$$

in which *T* is the temperature. As hexanoic acid is a weak acid, we assume that HCl dissociates in hexanoic acid similarly to water. Mole fraction is converted to mole ratio (*r*_{HCl}) and used to calculate an effective Henry's law coefficient using a dissociation constant of HCl in water of 10^{5.9} (following ref.⁵⁴)

$$H_{\text{HCl}} = \frac{r_{\text{HCl}} \times \rho_{\text{hex}} \times 10^{5.9}}{116}$$

in which ρ_{hex} is given by⁵⁵:

$$\rho_{\text{hex}} = (-5.01 \times 10^{-7} \times T^2 - 5.23 \times 10^{-4} \times T + 1.12) \times 1,000$$

The rates of the heterogeneous reactions are then calculated in the kinetics parameterization⁴¹ using this new value of Henry's law for HCl solubility in hexanoic acid. Because organic acids are weak acids, we assume that the acidity in a mixed organic/sulfuric acid solution would be determined largely by the sulfuric acid content. We do not consider the possible increase in pH owing to interactions of these organics with sulfuric acid and assume such changes to be small.

A caveat of this approach is that, in principle, the effective Henry's law best applies to dilute solutions so that some uncertainty occurs for strong solutions but laboratory data suggest that this is a small effect for our purposes⁸.

Observations

We use the MLS Level 2, version 5 PressureZM measurement product for O₃, HCl, HNO₃ and ClO data⁵⁶ to analyse mid-latitude (30–50° S) and polar (70–80° S) time series at 68 hPa as well as O₃ and ClO vertical profiles between 30° S and 50° S. We use the Level 2, version 5 PressureGrid measurement product for HCl maps. MLS has the benefit of daily measurements with few data gaps and allows for comprehensive temporal comparison with the model over all months in 2020. However, note that the ClO measurements at lower levels (68–147 hPa) are subject to a known negative bias. At 68 hPa, the bias is relatively small and has been reduced in version 5 compared with the previous version 4.2. It is therefore recommended⁵⁶ that day minus night measurements be used to reduce the bias. However, for the purposes of this paper in which comparison with model weekly average output is required and absolute values are less important as opposed to anomalies, we opted to use the averages of MLS day and night data. This also has the extra benefit of not having to account for further biases in the polar region for the MLS day minus night product.

Also, we use the ACE-Fourier transform spectrometer (FTS) version 4.1 data⁵⁷ for ClONO₂ and HOCl time series at 68 hPa and between 30° S and 50° S for mid-latitudes and 70° S and 80° S for polar conditions. We also use ACE for vertical profiles of ClONO₂ and HCl during June and July between 30° S and 50° S. The use of ACE HCl data here maximizes altitude coverage. ACE has sporadic spatial coverage for specific latitude ranges. Therefore, for the time series of ClONO₂, monthly averages of the available daily data for each month are constructed. For example, there is no data coverage between 30° S and 50° S in May and September. ACE quality control is performed by removing data points that lie outside three standard deviations of the mean values, as suggested for this data product⁵⁷.

Article

ACE and model data are interpolated onto a regular grid that coincides with the MLS pressure grid product to allow for appropriate comparison between datasets.

Data availability

All data used in this study are publicly available. MLS data: <https://disc.gsfc.nasa.gov/datasets?page=1&source=Aura%20MLS>; ACE-FTS data: <http://www.ace.uwaterloo.ca> (with registration: <https://database.scisat.ca/l2signup.php>); CESM1-CARMA: <https://doi.org/10.7910/DVN/GHNJQA>.

Code availability

The model used in this study can be accessed at <https://www2.cesm.ucar.edu/models/cesm1.2/cesm/doc/usersguide/x290.html>. The changes described herein for the kinetics parameterization are available at <https://doi.org/10.7910/DVN/GHNJQA>.

51. Bardeen, C. G., Toon, O. B., Jensen, E. J., Marsh, D. R. & Harvey, V. L. Numerical simulations of the three-dimensional distribution of meteoric dust in the mesosphere and upper stratosphere. *J. Geophys. Res.* **113**, D17202 (2008).
52. Toon, O. B., Turco, R. P., Westphal, D., Malone, R. & Liu, M. A multidimensional model for aerosols: description of computational analogs. *J. Atmos. Sci.* **45**, 2123–2143 (1988).
53. Rienecker, M. M. et al. *Technical Report Series on Global Modeling and Data Assimilation: The GEOS-5 Data Assimilation System-Documentation of Versions 5.0.1, 5.1.0, and 5.2.0* Vol. 27 (National Aeronautics and Space Administration, Goddard Space Flight Center, 2008).

54. Trummel, A., Lipping, L., Kaljurand, I., Koppel, I. A. & Leito, I. Acidity of strong acids in water and dimethyl sulfoxide. *J. Phys. Chem. A* **120**, 3663–3669 (2016).
55. Ghatee, M. H., Ghanavati, F., Bahrami, M. & Zolghadr, A. R. Molecular dynamics simulation and experimental approach to the temperature dependent surface and bulk properties of hexanoic acid. *Ind. Eng. Chem. Res.* **52**, 3334–3341 (2013).
56. Livesey, N. J. et al. Version 5.0x Level 2 and 3 data quality and description document. *Jet Propulsion Laboratory* <http://mhs.jpl.nasa.gov> (2020).
57. Boone, C. D., Bernath, P. F., Cok, D., Jones, S. C. & Steffen, J. Version 4 retrievals for the atmospheric chemistry experiment Fourier transform spectrometer (ACE-FTS) and imagers. *J. Quant. Spectrosc. Radiat. Transf.* **247**, 106939 (2020).

Acknowledgements S.S. and K.S. are partly supported by NSF 1848863. D.K. was financed in part by NASA grant 80NSSC19K0952. P.Y. is supported by the National Natural Science Foundation of China (42175089, 42121004). D.M.M. is supported by NOAA base and climate funding. The CESM project is supported by the National Science Foundation and the Office of Science (BER) of the U.S. Department of Energy. We gratefully acknowledge high-performance computing support from Cheyenne (<https://doi.org/10.5065/D6RX99HX>) provided by NCAR's Computational and Information Systems Laboratory, sponsored by the National Science Foundation.

Author contributions S.S. and K.S. contributed equally and are co-first authors of this study. S.S., K.S., P.Y. and D.M.M. designed the initial work. K.S. analysed the data and refined the study design and produced the figures. S.S. drafted the initial text. K.S., D.M.M., D.K., A.R.R. and P.W. contributed substantially to the interpretation of findings and to the revisions of the manuscript.

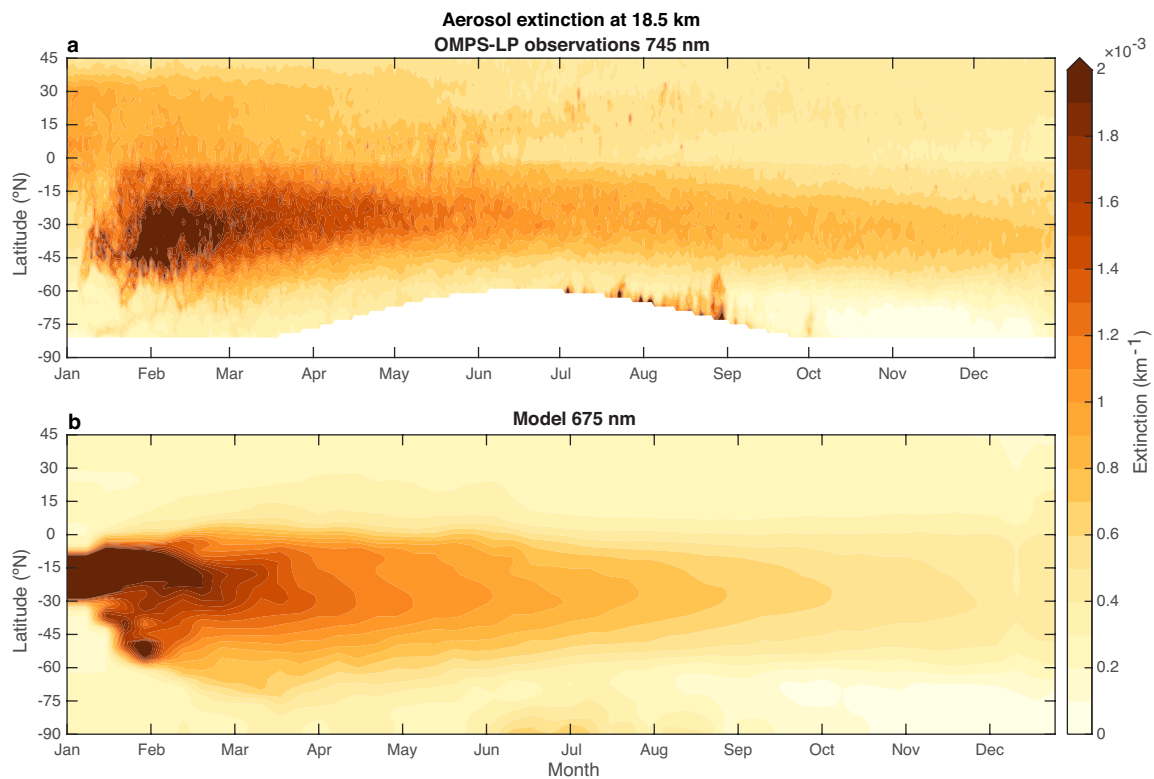
Competing interests The authors declare no competing interests.

Additional information

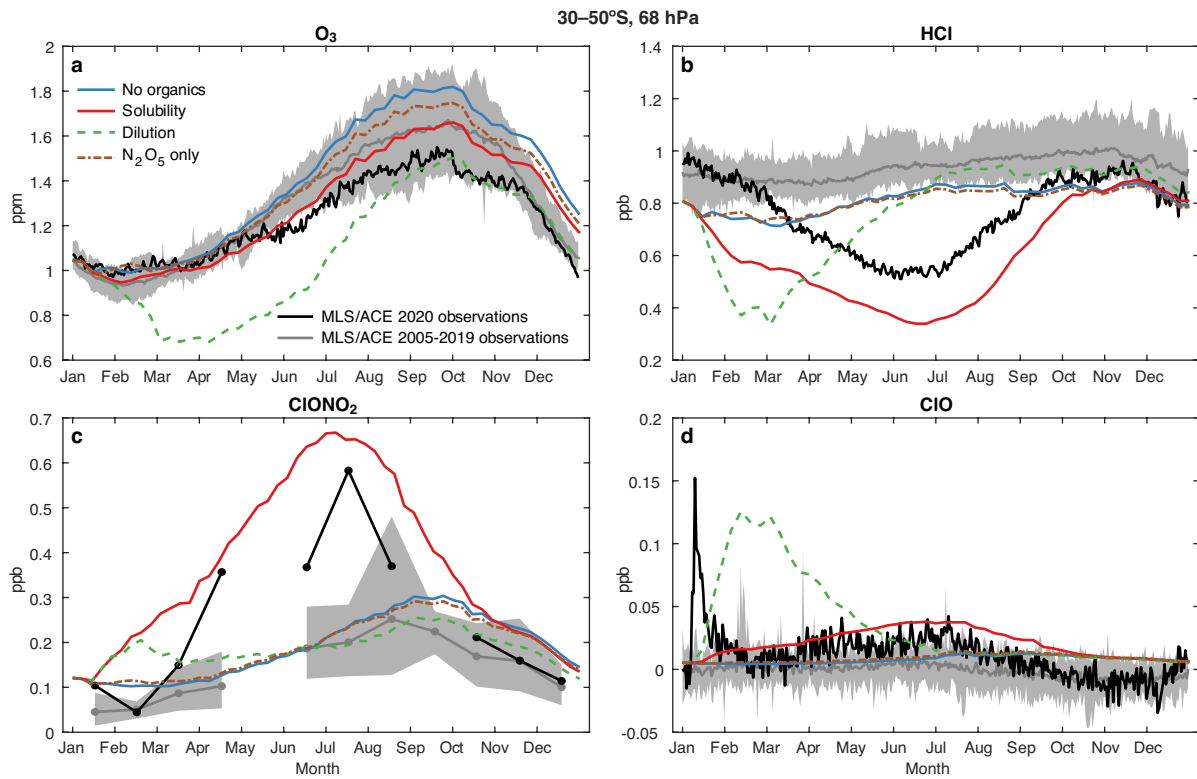
Correspondence and requests for materials should be addressed to Susan Solomon or Kane Stone.

Peer review information Nature thanks Clare Paton-Walsh and the other, anonymous, reviewer(s) for their contribution to the peer review of this work.

Reprints and permissions information is available at <http://www.nature.com/reprints>.

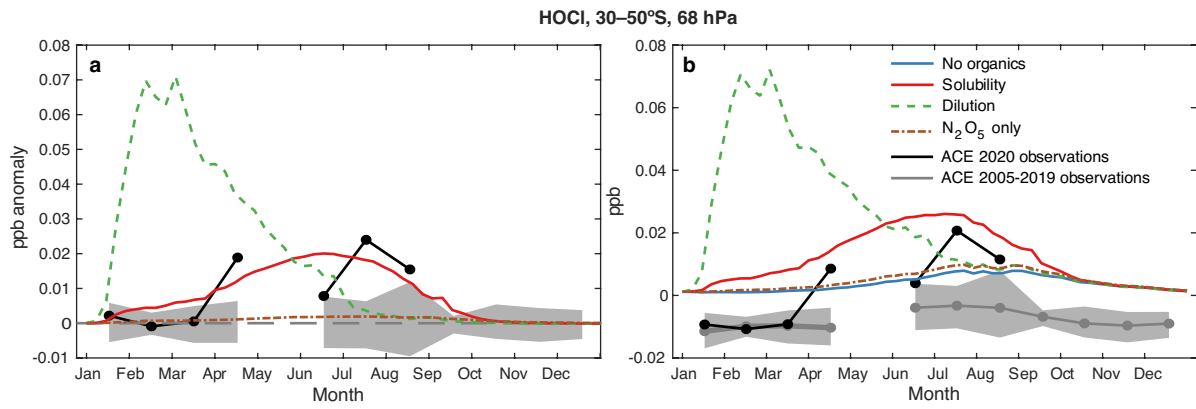


Extended Data Fig. 1 | Modelled and observed aerosol extinction at 18.5 km. The time evolution of aerosol extinction (km^{-1}) is shown at 18.5 km for Ozone Mapping and Profiler Suite (OMPS) observations (for 745 nm, **a**) and in the model (for 675 nm, **b**) in 2020.



Extended Data Fig. 2 | Observed and modelled 2020 absolute abundances for chemical species from 30–50° S at 68 hPa. Grey shaded regions show the ranges of 24-h averaged satellite data from the climatologies of satellite observations (in mixing ratio units) before 2020 (daily O_3 , HCl and ClO from MLS and monthly $ClONO_2$ from ACE) and the grey line shows their averages, whereas black lines show the observed values for 2020. Other coloured lines

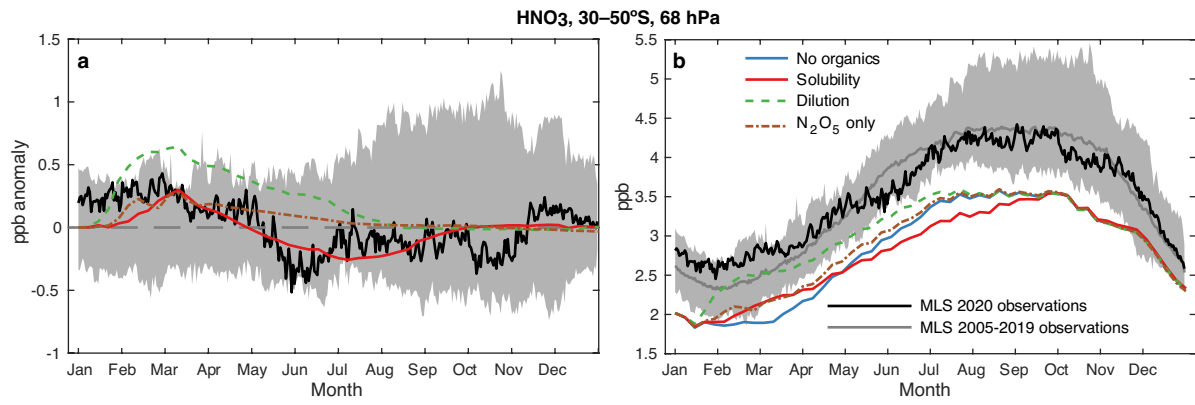
show model-calculated abundances for the no organics control run (blue line) and for three model test cases: including only N_2O_5 hydrolysis on the aerosols (dashed brown line), considering the added organic material as a dilution factor (green dashed line) and considering the adopted solubility of HCl in organic acid particles (red line). Corresponding anomalies are shown in Fig. 2.



Extended Data Fig. 3 | Observed and modelled monthly averaged anomalies (a) and mixing ratios (b) for HOCl (from ACE) for 30–50° S at 68 hPa.

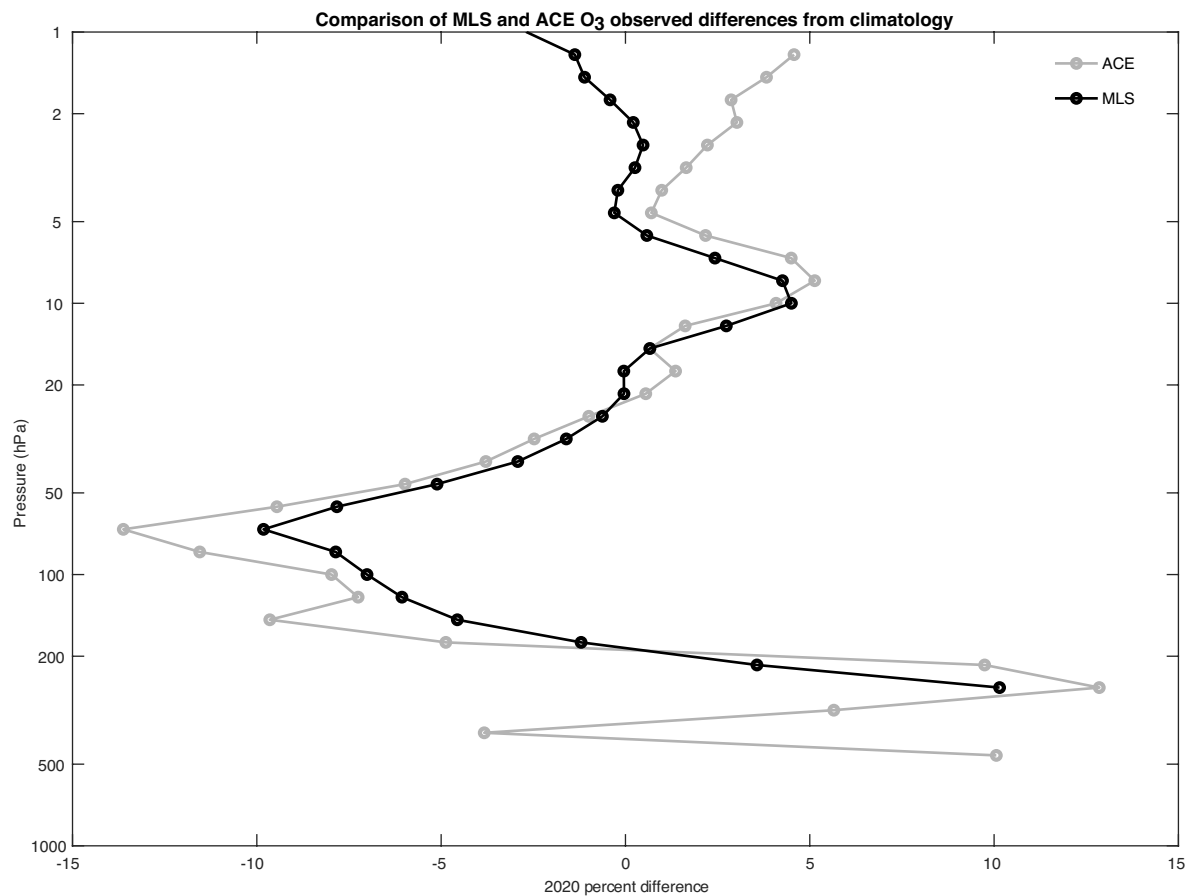
Grey shaded regions show the ranges of 24-h averaged satellite data from the climatology before 2020, whereas black lines show the observed values for 2020. Other coloured lines show calculated values for 2020 for the no organics

control run (blue line) and for three model test cases: including only N₂O₅ hydrolysis on the aerosols (dashed brown line), considering the added organic material as a dilution factor (green dashed line) and considering the adopted solubility of HCl in organic acid particles (red line).



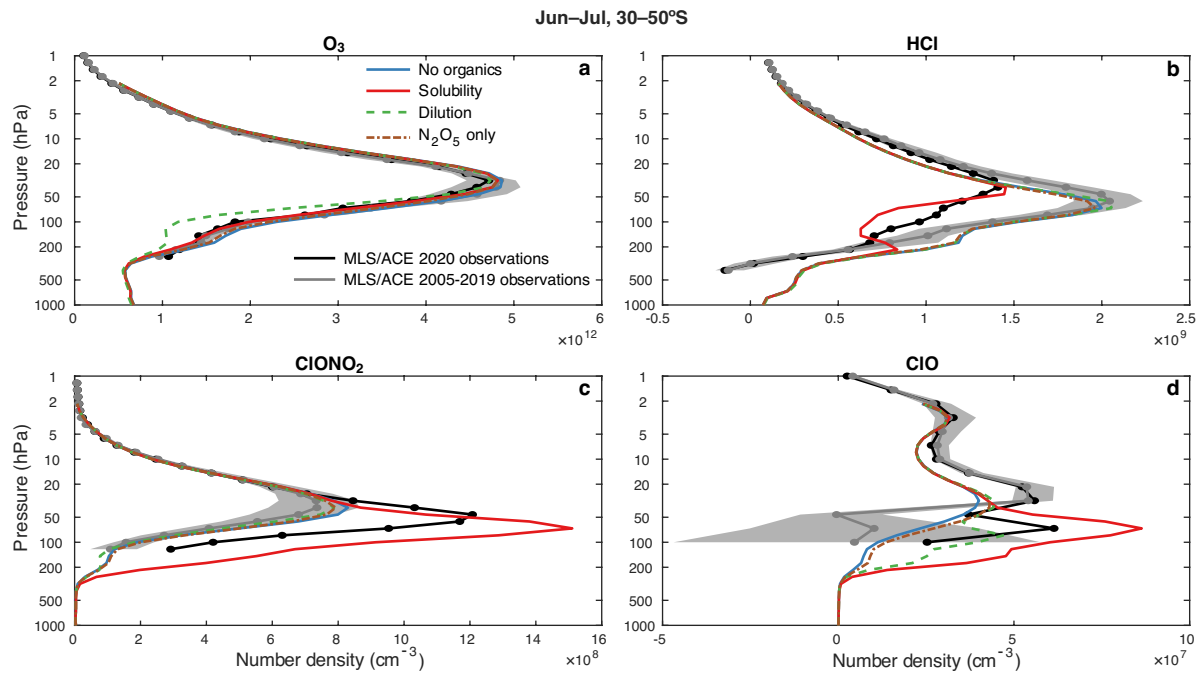
Extended Data Fig. 4 | Observed and modelled anomalies (a) and mixing ratios (b) for HNO₃ (from MLS) for 30–50° S at 68 hPa. Grey shaded regions show the ranges of 24-h daily averaged satellite data from the climatology before 2020, whereas black lines show the observed values for 2020. Other coloured lines show calculated values for 2020 for the no organics control run

(blue line) and for three model test cases: including only N₂O₅ hydrolysis on the aerosols (brown dashed line), considering the added organic material as a dilution factor (dashed green line) and considering the adopted solubility of HCl in organic acid particles (red line).



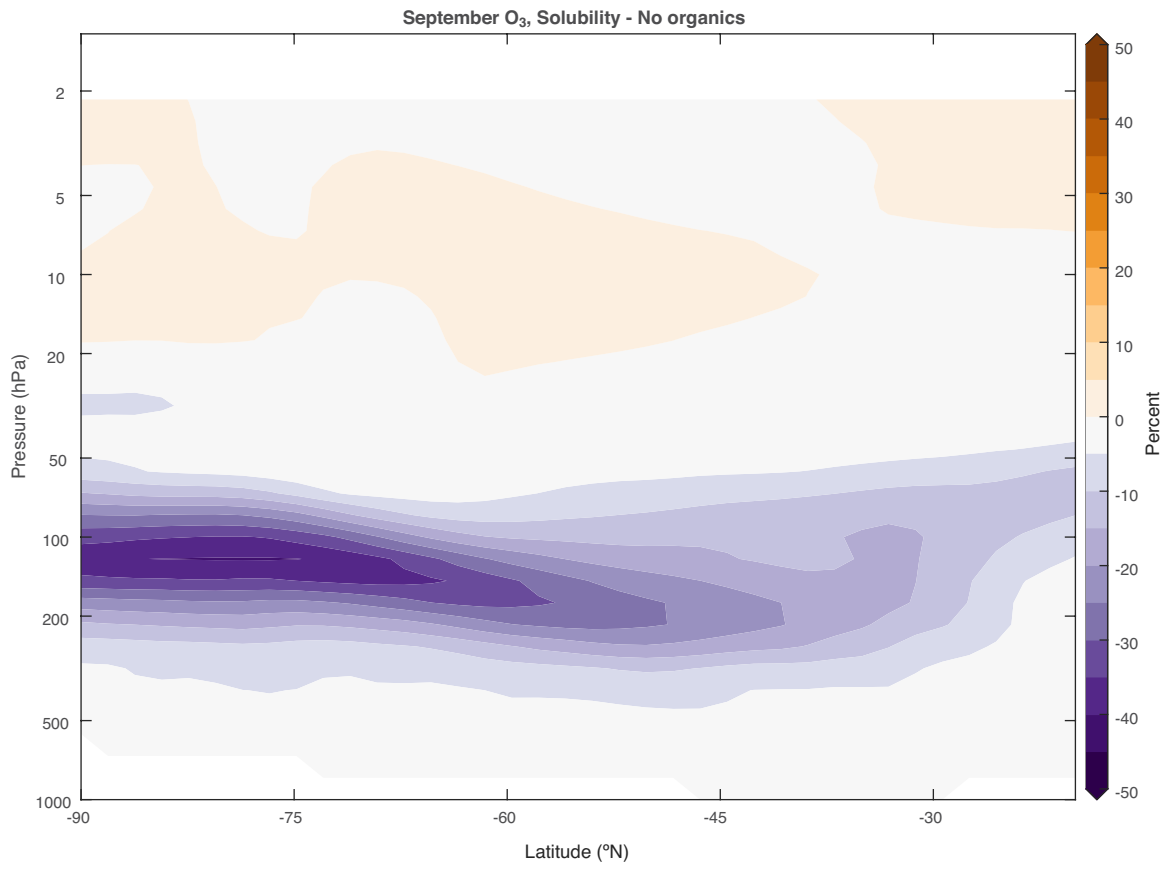
Extended Data Fig. 5 | Percent ozone anomalies for 30–50° S on coincident days of measurement for ACE and MLS during June–July 2020. Data for each satellite have been normalized by their respective climatologies. Note that

there are differences in spatial and temporal sampling between the two instruments. Black line shows MLS data while grey line shows ACE data interpolated onto the MLS pressure grid.

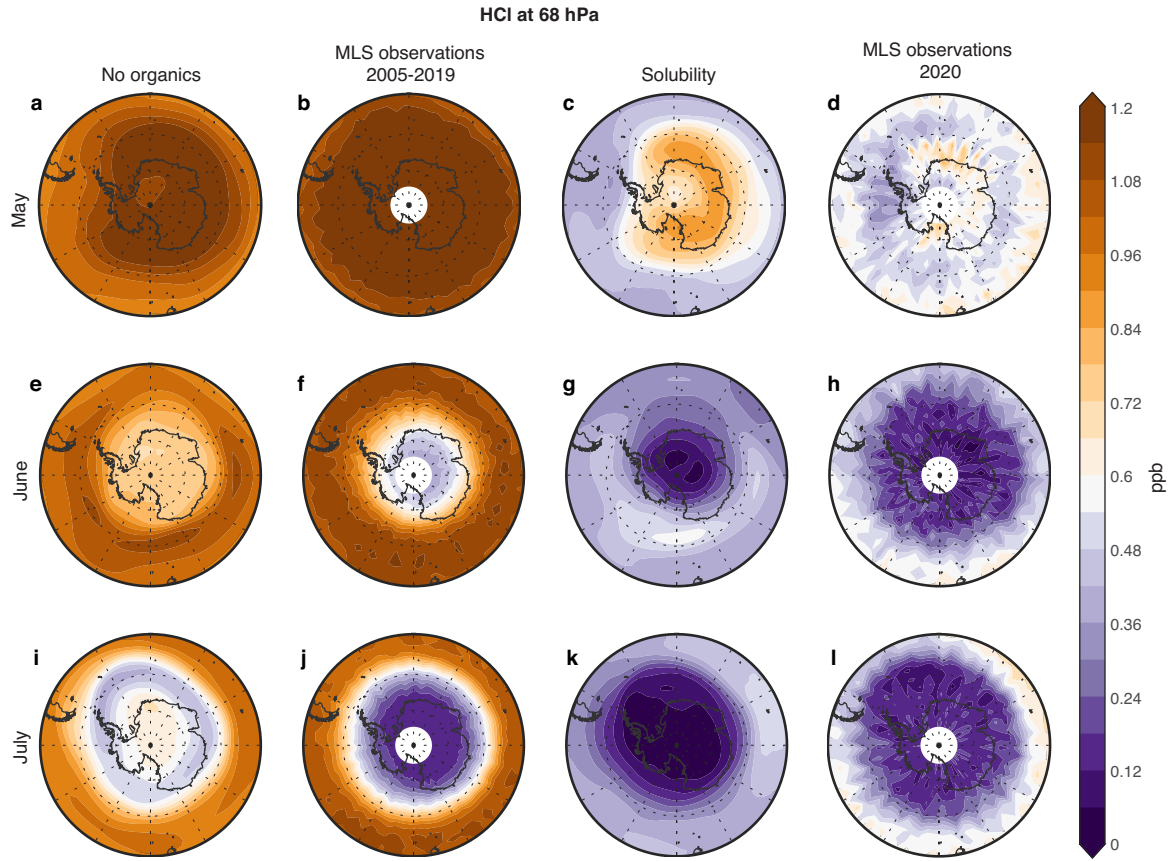


Extended Data Fig. 6 | Observed and modelled vertical profile absolute abundances for chemical species from 30–50° S in June–July of 2020. Grey shaded regions show the ranges of 24-h averaged satellite anomalies (in number density units) in years before 2020 (daily O_3 and ClO from MLS and HCl and ClONO_2 from ACE) and the grey line shows their averages, whereas black lines show observed abundances for 2020. Other coloured lines

show calculated values for 2020 for the no organics control run (blue line) and for three model test cases: including only N_2O_5 hydrolysis on the aerosols (brown dashed line), considering the added organic material as a dilution factor (green dashed line) and considering the adopted solubility of HCl in organic acid particles (red line). Corresponding anomalies are shown in Fig. 3.



Extended Data Fig. 7 | Distribution of calculated ozone loss in September 2020. Percentage change in model-calculated ozone as a function of latitude and height for the oxidized organics solubility model case is shown, as compared with the no organics control run.



Extended Data Fig. 8 | Contour maps of monthly mean HCl abundances (ppbv) at 68 hPa for observations and models. The modelled no organics control case is shown (left column), along with MLS-measured climatological

average from 2005–2019 (second from left), modelled oxidized organics solubility case (second from right) and MLS measurements for 2020 (right).